remote sensing

Article

Comparison of the Potential Impact to the Prediction of Typhoons of Various Microwave Sounders Onboard a Geostationary Satellite

Ke Chen [1,2,*] and Guangwei Wu [1]

[1] School of Electronic Information and Communications, Huazhong University of Science and Technology, Wuhan 430074, China; m202072155@hust.edu.cn
[2] Science and Technology on Multispectral Information Processing Laboratory, Wuhan 430074, China
* Correspondence: chenke@hust.edu.cn

Abstract: A microwave radiometer onboard a geostationary satellite can provide for the continuous atmospheric sounding of rapidly evolving convective events even in the presence of clouds, which has aroused great research interest in recent decades. To approach the problem of high-spatial resolution and large-size antennas, three promising geostationary microwave (GEO-MW) solutions—geostationary microwave radiometer (GMR) with a 5 m real aperture antenna, geostationary synthetic thinned aperture radiometer (GeoSTAR) with a Y-shaped synthetic aperture array, and geostationary interferometric microwave sounder (GIMS) with a rotating circular synthetic aperture array—have been proposed. To compare the potential impact of assimilating the three GEO-MW sounders to typhoon prediction, observing system simulation experiments (OSSEs) with the simulated 50–60 GHz observing brightness temperature data were conducted using the mesoscale numerical model Weather Research and Forecasting (WRF) and WRF Date Assimilation-Four dimensional variational (WRFDA-4Dvar) assimilation system for Typhoons *Hagibis* and *Bualoi* which occurred in 2019. The results show that the assimilation of the three GEO-MW instruments with 4 channels of data at 50–60 GHz could lead to general positive impacts in this study. Compared with the control experiment, for the two cases of *Bualoi* and *Hagibis*, GMR improves the average 72 h typhoon track forecast accuracy by 24% and 43%, GeoSTAR by 33% and 50%, and GIMS by 10% and 29%, respectively. Overall, the three GEO-MW instruments show considerable promise in atmospheric sounding and data assimilation. The difference among these positive impacts seems to depend on the observation error of the three potential instruments. GeoSTAR is slightly better than the other two GEO-MW sounders, which may be because it has the smallest observation error of the 4 assimilation channels. Generally, this study illustrates that the performance of these three GEO-MW sounders is potentially adequate to support assimilation into numerical weather prediction models for typhoon prediction.

Keywords: geostationary microwave observation; atmospheric sounding; synthetic aperture interferometric radiometer (SAIR); observing system simulation experiments (OSSEs); data assimilation

check for updates

Citation: Chen, K.; Wu, G. Comparison of the Potential Impact to the Prediction of Typhoons of Various Microwave Sounders Onboard a Geostationary Satellite. *Remote Sens.* **2022**, *14*, 1533. https://doi.org/10.3390/rs14071533

Academic Editors: Wan Wu, Likun Wang and Gad Levy

Received: 24 January 2022
Accepted: 20 March 2022
Published: 22 March 2022

1. Introduction

Microwave radiometers have operated on polar-orbiting satellites since the 1970s. The satellite radiance observations have contributed to steadily improving weather forecast accuracy through the direct assimilation into operational or research numerical weather prediction (NWP) models [1–5]. This is because they measure the thermodynamic state of the atmosphere even in the presence of clouds, which allows dynamic weather processes to be captured [6]. Due to the lack of in situ data in ocean regions, satellite observations are particularly significant in typhoon monitoring and prediction. However, a polar-orbiting satellite will at best pass over a given scene only twice in 24 h, which means that the most rapidly evolving phenomena, such as typhoons, are poorly sampled and therefore often poorly predicted. In contrast, due to the high temporal resolution and fixed observation view relative to the Earth's surface, a microwave sensor operating in geostationary orbit would overcome that obstacle, producing continuous microwave brightness temperature observations in a fixed domain [7].

The possibility of a microwave radiometer sounding the atmospheric state from a geostationary satellite has long been studied [8–10]. However, achieving adequate spatial resolution from 36,000 km is a long-standing problem. Several instrumental concepts using different technologies paved the way for future investigations. Early pioneering projects such as the Geosynchronous Microwave (GEM) sounder [11] and Geostationary Observatory for Microwave Atmospheric Sounding (GOMAS) [12] were based on traditional real aperture (RA) radiometer technologies similar to those used for low earth-orbiting (LEO) satellites. GEM used a 2 m diameter steerable Cassegrain reflector antenna, and GOMAS increased it to 3 m [13]. However, GEM and GOMAS could not achieve the required spatial resolution of ~50 km at the lowest atmospheric sounding frequency band of 50–60 GHz [14]. Recently, the Shanghai Aerospace Electronic Technology Institute (SAETI) designed a geostationary microwave radiometer (GMR) with a 5 m real aperture antenna as one possible implementation in the framework of the Chinese Fengyun geostationary satellite series FY-4 [15,16]. A prototype was manufactured, and the system design was verified through laboratory and imaging tests. Another alternative approach is synthetic aperture interferometric radiometer (SAIR) [17,18]. Active research is ongoing on this subject with two concepts under investigation: geostationary synthetic thinned aperture radiometer (GeoSTAR) [19] and geostationary interferometric microwave sounder (GIMS) [20]. GeoSTAR is a geostationary microwave (GEO-MW) sensor developed by the Jet Propulsion Laboratory (JPL) to provide high-spatial resolution soundings of the Earth's atmosphere. GeoSTAR uses a Y-shaped array incorporating hundreds of antenna feeds and receivers to sample the spatial Fourier spectrum of the radiometric field [21–24]. To reduce the number of SAIR antenna elements required, instead of the stationary array of GeoSTAR, a rotating thinned array concept GIMS was proposed by the National Space Science Center (NSSC), Chinese Academy of Sciences (CAS) [25,26]. GIMS applies a rotating circular antenna array of 70 elements working in time-sharing mode to realize the required spatial Fourier spectrum sample at 50–60 GHz with moderate system complexity at the expense of longer observation periods [27]. In summary, at present, GMR, GeoSTAR, and GIMS are the three promising GEO–MW sounder projects currently being studied. Although the three GEO-MW sounder projects based on different technology approaches have similar spatial resolutions, it is unknown whether there are similar impacts of assimilation of their data on NWP models.

NWP models and meteorological satellites have been the most important achievements in the field of meteorology in the past half-century, and their developments complement each other [28]. On the one hand, a large number of satellite observations from an increasing number of sensors have been assimilated directly into NWP models to improve forecasting performance; on the other hand, with the increasing accuracy of numerical weather forecasting, NWP models are also used for quality assessment, instrument design, and optimization of meteorological satellite observation systems. Among them, the observing system simulation experiment (OSSE) is one of the technical approaches [29–34]. The basic idea of an OSSE is to assimilate synthetic observations derived from an NWP model state assumed to represent the truth and then determine the impact on analyses and forecasts. To compare the potential impact of assimilation of the microwave observation data from GMR, GeoSTAR, and GIMSwith the prediction of typhoons, a reanalysis-based GEO-MW OSSE using the Weather Research and Forecasting (WRF) model and WRF Data Assimilation-Four dimensional variational (WRFDA-4DVar) assimilation system was conducted in this study. The observed brightness temperature of the 50–60 GHz oxygen absorption band with the three instrument configurations (GMR, GeoSTAR, and GIMS) was investigated. Typhoons *Hagibis* and *Bualoi* were selected as cases to analyze the impact of assimilation of the GEO-MW observations on typhoon track forecasts. Both typhoons were super typhoons in the Western Pacific, which have the greatest potential threat to China.

The remainder of this paper is organized as follows. Section 2 describes the data used in this study and Typhoons *Hagibis* and *Bualoi*. The OSSE framework and each of its components is detailed in Section 3. Section 4 details the methods used for simulating the three GEO-MW sounders and the comparison of their brightness temperature observation capabilities. The GEO-MW OSSE experimental setup and results are introduced in Section 5, with a summary presented in Section 6.

2. Data Used for Typhoons Hagibis and Bualoi

2.1. Data Used

The more realistic each of the OSSE components are, the more consistent the results will be with experiments using real observations. Thus, the fifth generation of the European Centre for Medium-Range Weather Forecasts (ECMWF) reanalysis (ERA-5) [35] data was used to generate the reference ('true') atmosphere or Nature Run (NR) of the GEO-MW OSSE and to evaluate the forecast skill scores. ERA-5, the successor to ERA-Interim, is the 5th major atmospheric reanalysis produced by the new generation of ensemble 4D-Var data assimilation (DA) technology, which represents 10 years of progress made in modeling and data assimilation since the production of ERA-Interim. The ERA-5 dataset provides high-resolution global reanalysis data of surface and upper-air parameters at an approximate 31 km global resolution on 137 levels reaching up to 0.01 hPa and a time resolution of 1 h.

In addition, another reanalysis dataset, Final Analysis (FNL) [36] data, was used to generate the background field of the WRFDA-4DVar assimilation and the initial field of the control experiment in the GEO-MW OSSE. Since 1999, FNL data have been provided as the final analysis by the National Oceanic and Atmospheric Administration (NOAA), the National Centers for Environmental Prediction (NCEP) located in Maryland for researchers. NCEP/FNL reanalysis data have a horizontal resolution of $1.0^{\circ} \times 1.0^{\circ}$ and temporal resolution of 6 h (observed at 0000 UTC, 0600 UTC, 1200 UTC, and 1800 UTC), which involves 31 pressure levels in the vertical direction, including 5 pressure levels (1000, 950, 925, 900, and 850 hPa) in the boundary layer.

To verify the track prediction of Typhoons *Hagibis* and *Bualoi*, the typhoon best tracks provided by the Tropical Cyclone Data Center (TCDC) of the China Meteorological Administration (CMA) [37,38] were used as the truth for typhoon prediction in the GEO-MW OSSE. Time, longitude, and latitude can be obtained from CMA data, which are available via https://tcdata.typhoon.org.cn/zjljsjj_zlhq.html (accessed on 21 March 2021).

2.2. Super Typhoon Hagibis

Hagibis (No. 1919) was named by the Japan Meteorological Agency (JMA) at 19:00 UTC on 5 October 2019, and it began a process of rapid strengthening. It was upgraded to a typhoon at approximately 21:00 UTC on 6 October and upgraded to a super typhoon by the CMA at 06:00 UTC on 7 October. It continued to strengthen and became the strongest typhoon since 2019 recognized by the CMA. Afterward, it passed near Anatahan Island in the northern Mariana Islands, turned north and moved north by east, and its intensity weakened slowly. It approached the Tokyo capital circle and landed off the coast of the Izu Peninsula, Japan, at approximately 10:00 UTC on 12 October. The CMA finally stopped numbering it at 8:00 on 13 October.

2.3. Super Typhoon Bualoi

The predecessor of *Bualoi* (No. 1921) was the tropical generated in the Northwest Pacific on 15 October, 2019. It was upgraded to a tropical storm and numbered 1921 by the JMA at approximately 13:00 UTC on 19 October. Since that time, Typhoon *Bualoi* steadily strengthened. The JMA and CMA upgraded it to a strong tropical storm at 00:00 UTC and 09:00 UTC on 27 October, respectively, and to a super typhoon on 22 October. *Bualoi* then began to weaken and gradually transformed into an extratropical cyclone. At 12:00 UTC on 25 October, the CMA discontinued forecasting on *Bualoi*.

3. Observing System Simulation Experimental Framework

3.1. Framework of the GEO-MW OSSE

The OSSE is an important means to develop and evaluate new observation systems. The basic principle of an OSSE is to assimilate the synthetic future spaceborne observation data derived from the Nature Run data, satellite orbit parameters, and instrument parameters and then evaluate the impact of new observations on analyses and forecasts [31]. The GEO-MW OSSE in this study was realized by the WRF model and WRFDA-4DVar assimilation system. The flowchart of the GEO-MW OSSE is shown in Figure 1, including the following seven main steps:

1. ERA-5 reanalysis data are used as the initial fields and boundary conditions to run the WRF model to forecast the Nature Run data.
2. The Radiative Transfer (RT) model takes in a set of input atmosphere physics parameters provided by the Nature Run and calculates upwelling brightness temperature (TB) emerging from the top of the atmosphere.
3. The upwelling TB is input into the GEO-MW observation models of GMR, GeoSTAR, and GIMS with the geostationary orbit parameters and the three instrument parameters to simulate the observed brightness temperature (TA).
4. NCEP/FNL reanalysis data are used as the initial fields to run the WRF model, and the 6th-hour prediction field is used as the background field of WRFDA-4DVar assimilation.
5. The simulated GEO-MW observation TA data of GMR, GeoSTAR, and GIMS are assimilated by the WRFDA-4DVar assimilation system to obtain the analysis fields.
6. The 72-h predictions are obtained from the WRF model initialized with the analysis fields (GEO-MW assimilation experiments) and the background field (control experiment).
7. The impacts of the GEO-MW observation data assimilation are evaluated by comparing the predicted typhoon tracks with the best typhoon tracks provided by the CMA.

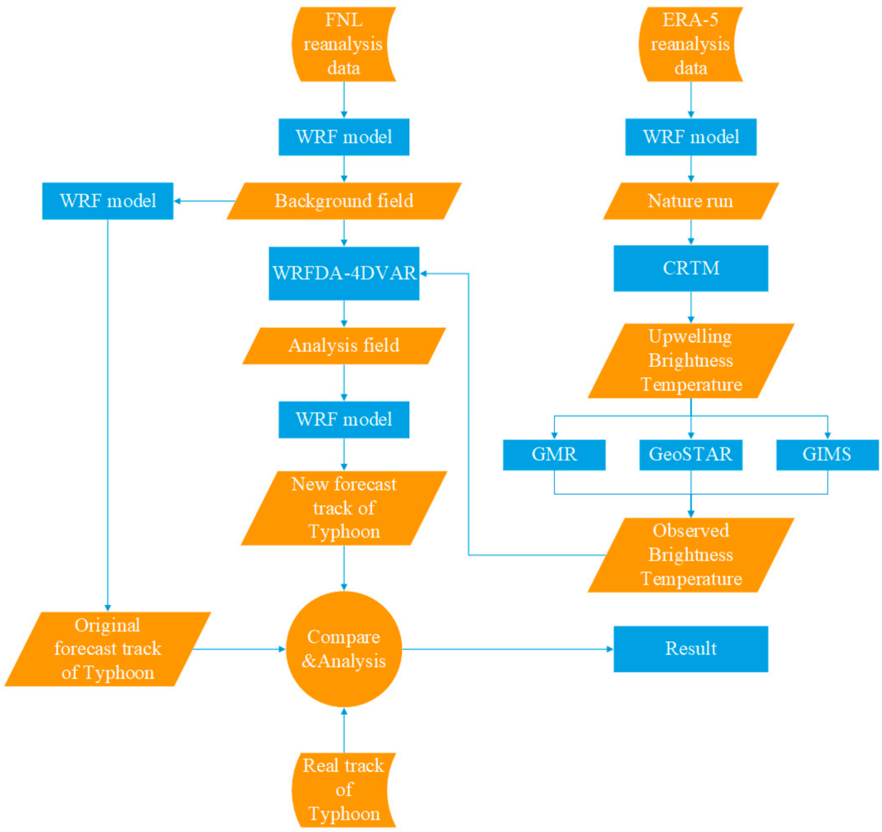

Figure 1. Geostationary orbit microwave observation system simulation experimental framework.

3.2. Nature Run and WRF Model

The National Center for Atmospheric Research (NCAR), the NCEP, and other American scientific research institutions developed a unified meteorological model called the WRF model. The WRF model is a fully compressible, nonhydrostatic model (with a hydrostatic option). WRF V3.8.1 released on 12 August 2016 was used in this study. The parameterization scheme of the WRF model is shown in Table 1.

Table 1. WRF physical parameterization scheme.

Physical Process Type	Parametric Scheme	Parameter
Microphysical process	Lin	mp_physics = 2
Longwave radiation process	RRTM	ra_lw_physics = 1
Shortwave radiation process	Dudhia	ra_sw_physics = 1
Land surface model	Noah	sf_surface_physics = 2
Boundary layer parameterization process	YSU	bl_pbl_physics = 1
Cumulus convection parameterization scheme	Kain-Fritsch	cu_physics = 1

The Nature Run used here is a two-week-long WRF forecast initialized with the ERA-5 reanalysis data. The WRF outputs saved every half hour were used to simulate all synthetic GEO-MW observations described below. For Typhoon *Bualoi*, the ERA-5 reanalysis data at 0600 UTC on 22 October 2019 were used as the initial field to run the WRF model forecast to 0600 UTC on 5 November 2019. For Typhoon *Hagibis*, the Nature Run data covers 0600 UTC on 8 October 2019 to 0600 UTC on 22 October 2019.

3.3. WRFDA-4DVar Assimilation

WRFDA was used in the GEO-MW OSSE to assimilate the synthetic GEO-MW observed brightness temperature data from GMR, GeoSTAR, and GIMS. WRFDA is a data assimilation system built within the WRF software framework and used for application in both research and operational environments. The WRFDA was developed and maintained by the Mesoscale and Microscale Meteorology (MMM) Laboratory of NCAR and is freely available to the general community, together with further documentation, test results, etc. WRFDA web page (http://www2.mmm.ucar.edu/wrf/users/wrfda/index.html (accessed on 21 March 2021)). WRFDA can assimilate various observation data that include satellite brightness temperature and is also suitable for use in a broad range of applications across scales ranging from kilometers for regional and mesoscale modeling to thousands of kilometers for global-scale modeling. Various assimilation schemes are supported in WRFDA, including 3DVar, 4DVar, and hybrid ensemble–variational (EnVar).

4DVar assimilation is an extension of 3DVar in the time dimension, considering that the characteristics of observation data change with time. 4DVar essentially solves the analysis field that best matches all effective observation data in the assimilation time window. Prior to 2006, the global 4D-Var data assimilation system was in operation in the leading global numerical weather forecasting centers [39–41]. In this study, 4DVar was employed because it assimilates all observation data within the assimilation time window at a fixed time step and is more suitable for assimilation of GEO-MW observation data with a high-temporal resolution. The data assimilation problem is solved by minimizing the cost function in the 4DVar scheme:

$$J(x) = \frac{1}{2}(x - x_b)^T B^{-1}(x - x_b) + \frac{1}{2}\sum_{i=0}^{n}(H_i(M_{0\to i}(x) - y_i)^T R_i^{-1}(H_i(M_{0\to i}(x) - y_i) + J_c \quad (1)$$

where x is the atmospheric state to be solved, x_b is the background state; B is the error covariance matrix of x_b; y_i is the observation at time i; H is the observation operator; R_i is the observational error covariance matrix at time i; $M_{0\to i}$ is the model integration from the analysis time to time i; and J_c is the weak constraint term based on the digital filter.

The system framework of WRFDA-4DVar is shown in Figure 2. The WRFDA system iteratively updates the background state x_b and finally obtains the analysis field x_a, which initializes the new prediction. It also supports updating boundary conditions, including side boundary updating and lower boundary updating.

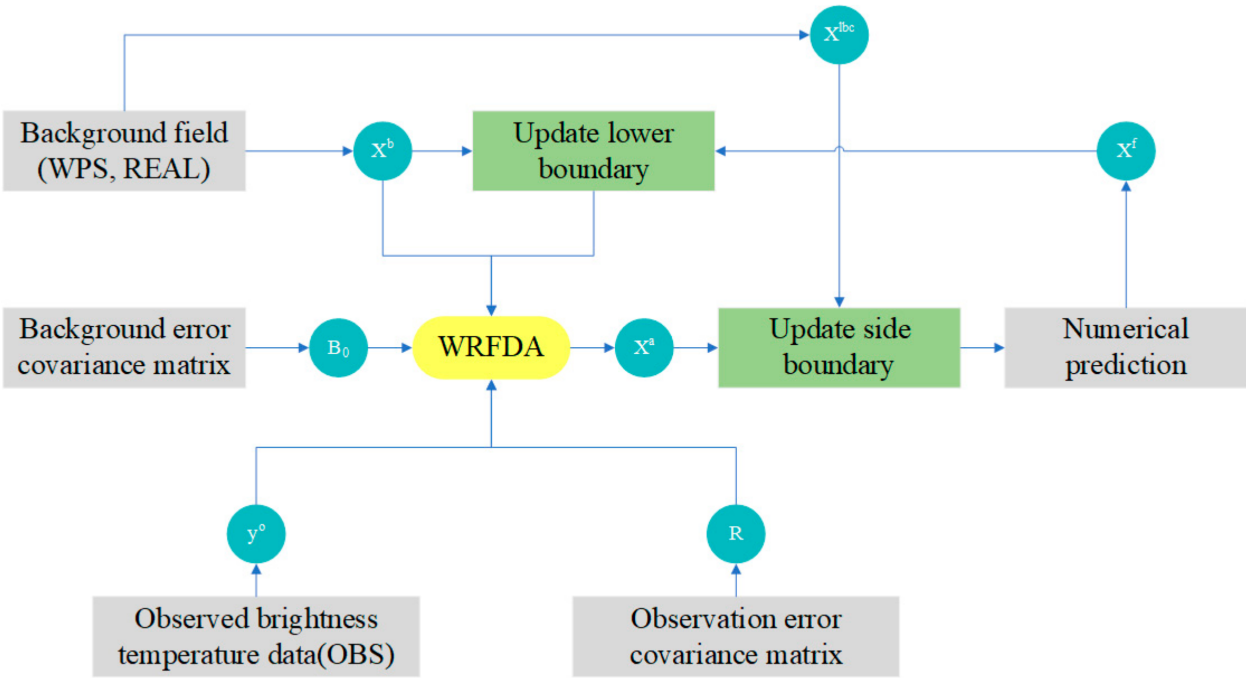

Figure 2. WRFDA-4DVar system framework.

4. Observation Simulations of GMR, GeoSTAR, and GIMS

It has long been recognized that a microwave radiometer onboard a geostationary satellite would be a powerful tool for weather prediction because it could sound the vertical profiles of temperature and humidity inside clouds by frequently monitoring a fixed area and acquiring high-temporal resolution on wide-range Earth observations. The geostationary microwave observations investigated in this study were synthetically generated by the simulated microwave brightness temperature data of GMR, GeoSTAR, and GIMS. In the GEO-MW OSSE, 8 channels in the 50–60 GHz oxygen absorption band were chosen, whose center frequencies are listed in Table 2. The 50–60 GHz band sounds atmospheric temperature by the absorption/emission of microwave radiance. Figure 3 shows the 50.3 GHz simulated brightness temperature map of the full-Earth disk outputted from the observation process model of GMR, GeoSTAR, and GIMS.

Table 2. Channels for simulated GEO-MW brightness temperature.

Channel	1	2	3	4	5	6	7	8
center frequency (GHz)	50.3	51.76	52.8	53.596	54.4	54.94	55.5	57.29

Passive microwave remote sensing uses a microwave radiometer to detect and receive the electromagnetic radiation of the measured object in the microwave band. From a mathematical point of view, the observation process of a microwave atmospheric sounding radiometer can be regarded as a mapping from atmospheric physical states to the observed brightness temperature seen by the sensor. The following three steps are used to establish this mapping. First, the "true" atmospheric states are obtained from the Nature Run. Second, the atmospheric state parameters are input into the Community Radiative Transfer

Model (CRTM) to calculate the upwelling brightness temperature TB at the top of the atmosphere. Finally, a sensor simulator composed of coordinate transformation, system response, and data processing is used to simulate the observed brightness temperature TA. GMR is a traditional real aperture radiometer, GeoSTAR is a SAIR with a stationary Y-shaped array, and GIMS is a SAIR with a rotating thin circular array. The three GEO-MW sensors have different technical systems and observation data processes; therefore, it is necessary to establish three different simulators to obtain the observed TA by the GMR, GeoSTAR, and GIMS, introduced in detail in Section 4.2.

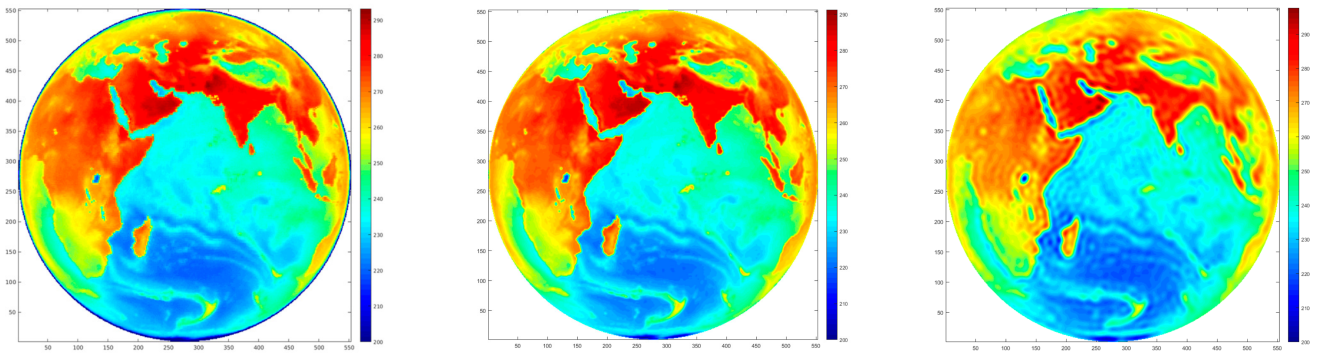

(**a**) (**b**) (**c**)

Figure 3. 50.3 GHz simulated brightness temperature map of the full-Earth disk for (**a**) GMR, (**b**) GeoSTAR, and (**c**) GIMS.

4.1. Upwelling Brightness Temperature TB

Electromagnetic radiation transfer in the atmosphere involves the absorption, emission, and scattering of various gas components and hydrometeors, whose mathematical model is generally expressed by the differential radiation transfer equation (DRTE). The simulation of the upwelling brightness temperature TB at the top of the atmosphere is realized using the RT model to obtain the numerical solution of the DRTE.

CRTM, developed at the Joint Center for Satellite Data Assimilation (JCSDA) in the United States, has been supporting satellite product retrievals, radiance validation for satellite programs, and satellite radiance assimilation for NWP, including WRFDA-4DVar. In 2008, the CRTM simulated radiance was directly compared with the observed microwave radiances of the NOAA-18 Advanced Microwave Sounding Unit-A (AMSUA), Microwave Humidity Sounder (MHS) sensors. The simulated and observed brightness temperature fields were in good agreement for all microwave channels (on the order of 1–2 K bias) [42]. In 2013, the CRTM simulated brightness temperature was used to evaluate the accuracy of the Advanced Technology Microwave Sounder (ATMS) brightness temperature data. The results showed that the brightness temperature biases for temperature sounding channels were below 1 K [43]. Therefore, the CRTM was used to calculate the upwelling brightness temperature TB in the GEO-MW OSSE. The atmospheric state parameters in Nature Run, including vertical profiles of pressure, temperature, moisture, and hydrometeor content (cloud liquid water, rain, ice, snow, and graupel) with a temporal resolution of 0.5 h, were used as inputs for the CRTM. The simulated upwelling brightness temperature TB field of Typhoon Hagibis for all 8 channels is shown in Figure 4A–H. The corresponding TA of the three GEO-MW sounders is shown in Figure 4.

4.2. Simulation of the Observed Brightness Temperature TA of GMR, GeoSTAR, and GIMS

In the GEO-MW OSSE, the 50–60 GHz observed brightness temperature TA of the three candidate GEO-MW sounders, GMR, GeoSTAR, and GIMS, were simulated. In the 50–60 GHz band, GMR is a microwave radiometer with a real aperture antenna with 5 m diameter, GeoSTAR is a SAIR with a stationary 312-element Y-shape array with a ~3.7 m array aperture, and GIMS is a SAIR with a rotating 70-element circular array with a 3.7 m diameter. The simulation configurations of the three GEO-MW sounders are listed in Table 3, including the bandwidth BW, noise figure NF, integration time τ, number of array elements N, minimum spacing between array elements d, aperture size of antenna/array D, and image period T. The simulation process of each GEO-MW sounder is described in detail as follows.

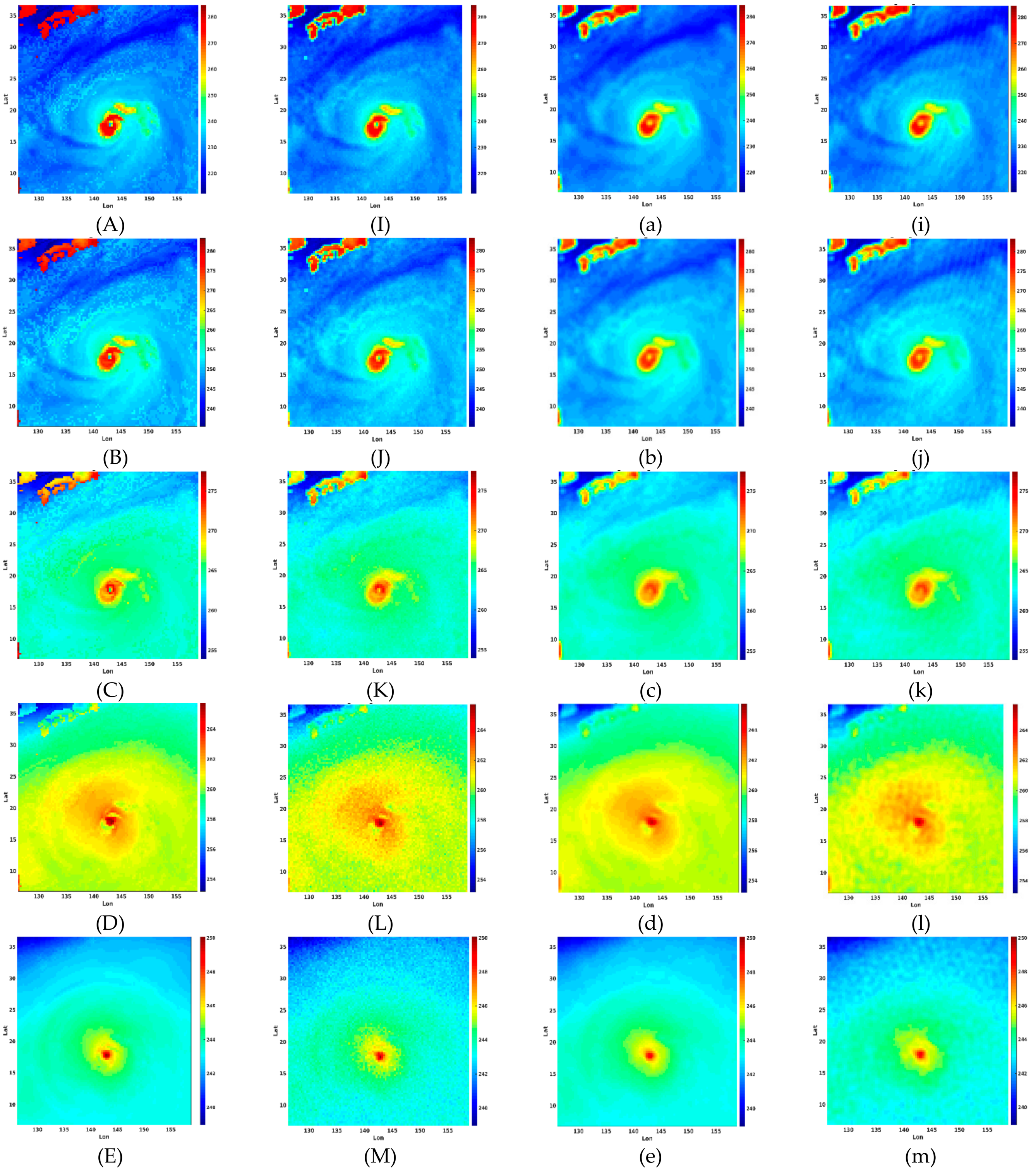

Figure 4. *Cont.*

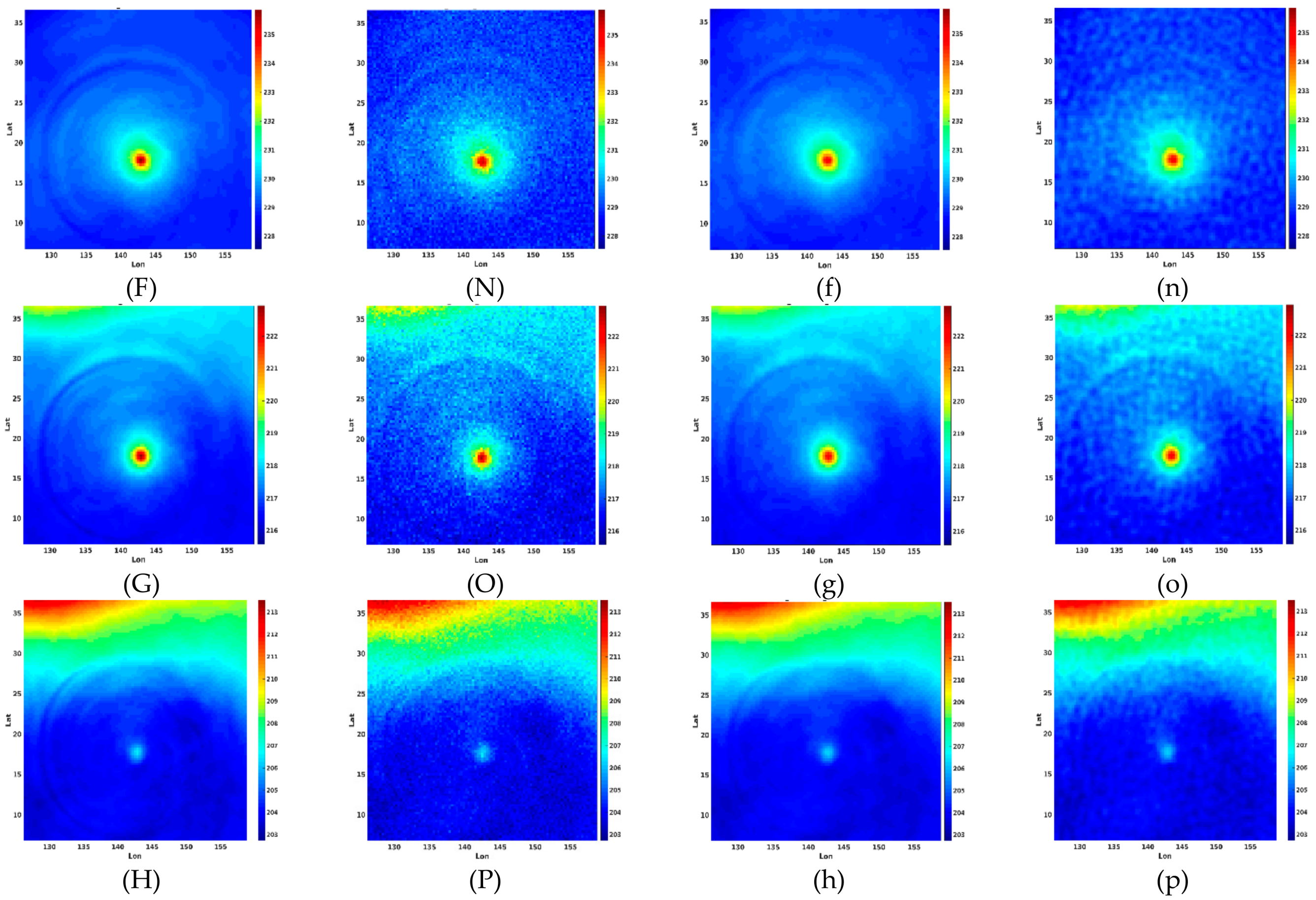

Figure 4. Simulated upwelling brightness temperature TB (**A**–**H**) and observation TA of GMR (**I**–**P**), GeoSTAR (**a**–**h**), and GIMS (**i**–**p**). (**A**,**I**,**a**,**i**) represents channel-1 50.3 GHz, (**B**,**J**,**b**,**j**) represents channel-2 51.76 GHz, (**C**,**K**,**c**,**k**) represents channel-3 52.8 GHz, (**D**,**L**,**d**,**l**)represents channel-4 53.596 GHz, (**E**,**M**,**e**,**m**) represents channel-5 54.4 GHz, (**F**,**N**,**f**,**n**) represents channel-6 54.94 GHz, (**G**,**O**,**g**,**o**) represents channel-7 55.5 GHz, and (**H**,**P**,**h**,**p**) represents channel-8 57.29 GHz.

Table 3. The simulation configurations of the three GEO-MW sounders.

Instrument	BW (MHz)	NF (dB)	τ (s)	N	d (cm)	D (m)	T (s)
GMR	180–400	5	0.04	/	/	5	~600
GeoSTAR	200	5	300	312	2.1	3.7	300
GIMS	200	5	1	70	1.87	3.7	~300

4.2.1. Geostationary Microwave Radiometer (GMR)

A real aperture radiometer is mainly composed of antennas and receiver channels. The measured antenna temperature of the real aperture radiometer GMR at location $(\theta_0, \varphi_0\ )(\mathrm{TA}(\theta_0, \varphi_0))$ can be formulated as the integration of the products of the upwelling brightness temperature TB image and the normalized antenna gain pattern G_n plus the system noise ΔT_{rms} [44]:

$$T_A(\theta_0, \varphi_0) = \int TB(\theta, \varphi) G_n(\theta_0, \varphi_0; \theta, \varphi) d\Omega + \Delta T_{rms} \tag{2}$$

where (θ, φ) denotes the elevation and azimuth angles of the point on the Earth's surface in the spherical coordinate system of the antenna, respectively, $T_A(\theta_0, \varphi_0)$ represents observed brightness temperature at (θ_0, φ_0), $G_n(\theta_0, \varphi_0; \theta, \varphi)$ represents gain in the field of view (θ, φ) when the antenna is aligned with (θ_0, φ_0), Ω is unit solid angle, ΔT_{rms} is random noise. Equation (2) is a standard signal model for a real aperture microwave radiometer, which presents the intrinsic degradation quality in the GMR observation process. The main influence on the observed brightness temperature TA data is the smoothing effect introduced by the limited antenna beam main lobe width and the system noise. In the model, it is usual practice that the system noise ΔT_{rms} is simulated by white Gaussian noise, whose standard deviation is approximately equal to the noise-equivalent brightness temperature (NEΔT) of each frequency channel of the GMR. The simulated GMR uses a circular aperture parabolic antenna with a 5 m diameter, whose antenna gain pattern G_n is calculated using Equation (3).

$$G_n(\theta, \varphi) = 2J_1\left(\frac{\pi D}{\lambda} sin\theta\right) / \left(\frac{\pi D}{\lambda} sin\theta\right) \tag{3}$$

where J_1 represents the first-order Bessel function, D is the antenna diameter, and λ is the wavelength. Because the circular aperture antenna is symmetrical in the azimuth angle φ, its pattern G_n is only a functsion of the elevation angle θ. Figure 5a,f shows the simulated 2-D and E-plane 1-D antenna patterns of GMR at 50.3 GHz, and the corresponding 3-dB beamwidths are 0.087°.

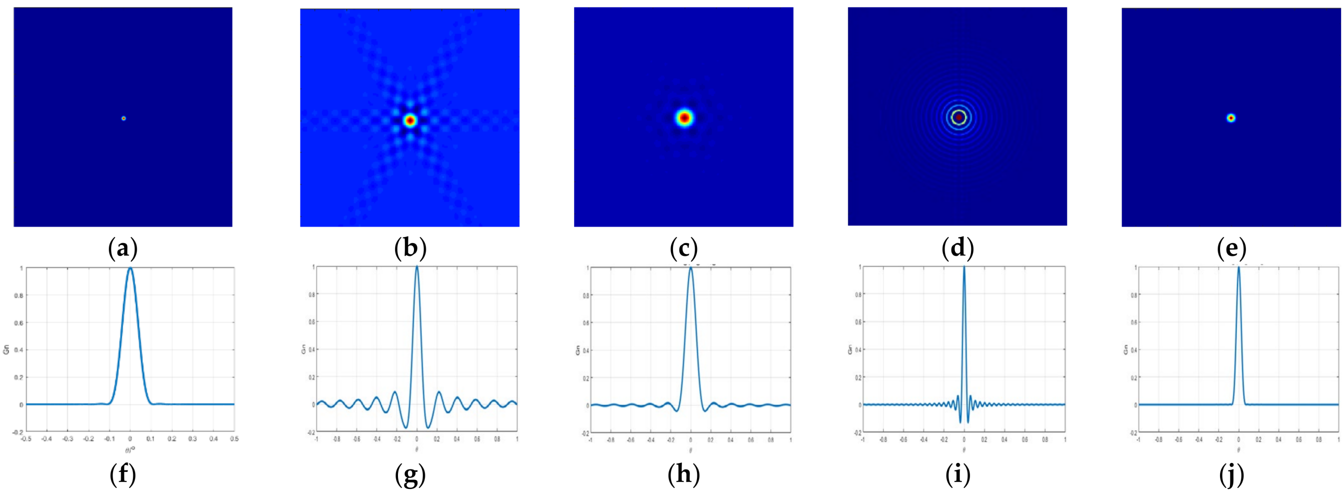

Figure 5. Simulated 2-D antenna pattern of RA and synthetic AF of SAIR at 50.3 GHz. (**a**) GMR, (**b**) GeoSTAR with a rectangular window, (**c**) GeoSTAR with a Blackman window, (**d**) GIMS with a rectangular window, and (**e**) GIMS with a Blackman window. The simulated 1-D antenna pattern and synthetic AF of SAIR. (**f**) GMR, (**g**) GeoSTAR with a rectangular window, (**h**) GeoSTAR with a Blackman window, (**i**) GIMS with a rectangular window, and (**j**) GIMS with a Blackman window.

To generate the simulated observation of GMR, first, the coordinates of each pixel of the upwelling brightness temperature TB are converted from the latitude and longitude coordinate system to the antenna spherical coordinate system of GMR, and then, $TB(\theta, \varphi)$, $G_n(\theta, \varphi)$, and ΔT_{rms} are substituted into Equation (2) to calculate the observed antenna brightness temperature TA. The simulated GMR antenna brightness temperature TA images of Typhoon Hagibis for all 8 channels are shown in Figure 4I–P.

4.2.2. Geostationary Synthetic Thinned Aperture Radiometer (GeoSTAR)

GeoSTAR is the first SAIR concept for GEO-MW atmospheric sounding. As illustrated in Figure 6a, GeoSTAR consists of a Y-shape array of 312 50–60 GHz antennas and receivers, where three linear arrays are offset 120° from each other. All of the antennas are pointed toward Earth. Unlike RA, SAIR measures the upwelling brightness temperature TB in the spatial frequency domain. This is achieved by the complex cross-correlations of the signals received by receiver pairs (so-called baseline pair) in a sparsely filled 2-D array, which is called the visibility function. Each baseline pair forms an interferometer, which measures a particular spatial harmonic of the brightness temperature distribution across the field of view. The spatial harmonic depends on the spacing between the antennas and the wavelength of the measured radiation. The visibility function is related to the brightness temperature of the observed scene as follows [44]:

$$V(u,v) = \iint_{\xi^2+\eta^2\leq 1} T'(\xi,\eta) r\left(-\frac{u\xi+v\eta}{f_0}\right) e^{-j2\pi(u\xi+v\eta)} d\xi d\eta \tag{4}$$

where V is visibility function, $(\xi,\eta) = (\sin\theta\cos\varphi, \sin\theta\sin\varphi)$ are the direction cosine coordinates, $(u,v) = (D_x/\lambda_0, D_y/\lambda_0)$ are the baseline components normalized to the wavelength $\lambda_0 = c/f_0$, with f_0 being the center frequency of the instrument, and $r(\tau)$ is the fringe washing function accounting for spatial decorrelation effects. $T'(\xi,\eta)$ is the modified brightness temperature, which is defined as follows when assuming identical antenna patterns:

$$T'(\xi,\eta) = \frac{TB(\xi,\eta)}{\sqrt{1-\xi^2-\eta^2}} \frac{|\mathrm{F}_n(\xi,\eta)|^2}{\Omega} \tag{5}$$

where TB is the scene's actual upwelling brightness temperature distribution, F_n is the modified antenna electric field pattern, and Ω is the antenna equivalent solid angle. The modified brightness temperature $T'(\xi,\eta)$ and the visibility function $V(u,v)$ are related by the Fourier transform in the ideal case, as indicated by Equation (4). Each baseline pair can sample two visibility points in the spatial frequency domain (so-called UV plane) by virtue of the conjugate symmetry property.

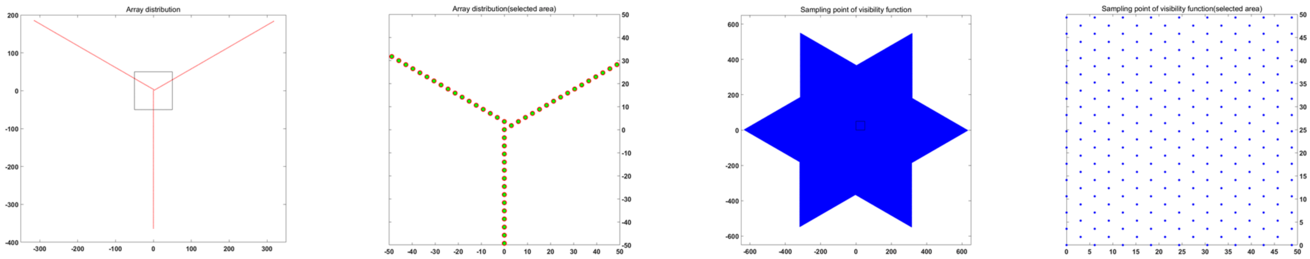

(**a**) (**b**) (**c**) (**d**)

Figure 6. The antenna array (**a**,**b**) (partial zoomed—in view) and resulting UV plane sampling pattern (**c**,**d**) (partial zoomed-in view) of GeoSTAR.

Figure 6a shows the distribution of elements in GeoSTAR's aperture plane, and Figure 6c shows the resulting samples in the UV plane. Figure 6b,d is the corresponding partial zoomed-in views. The smallest element spacing is 3.5 wavelengths (2.1 cm) for the 50–60 GHz band. The visibility function is essentially the 2-D Fourier transform of the 2-D brightness temperature field. The measurements made at these UV plane samples determine the coefficients of a 2-D Fourier series expansion of the brightness temperature field, and the field can then be reconstructed by an inverse Fourier transform as follows:

$$T'(\xi,\eta) = \iint W(u,v) V(u,v) e^{j2\pi(u\xi+v\eta)} du dv \tag{6}$$

where $W(u,v)$ is a window function used for weighting the visibility samples prior to inverse Fourier transformation for sidelobe suppression. In the actual case, the visibility functions are sampled at discrete points, and the scene brightness temperature distribution can be reconstructed by general inverse discrete Fourier transform (DFT) or inverse fast Fourier transform (FFT) routines.

The array factor (AF) of a SAIR is defined as Equation (7), which is also called the point spread function (PSF).

$$\mathrm{AF}(\xi,\eta) = \iint W(u,v)e^{j2\pi(u\xi+v\eta)}dudv \quad (7)$$

The window function $W(u,v)$ reduces the sidelobe level (SLL) of the AF and enhances the main beam efficiency, whereas, at the same time, it increases the 3-dB width of the main lobe. The AF in a SAIR has the same behavior as the antenna pattern in a traditional RA radiometer. Therefore, the angular resolution of SAIR is defined by the 3-dB beamwidth of the AF. Figure 5b,g shows the simulated 2-D and E-plane 1-D AF of GeoSTAR with a rectangular window at 50.3 GHz, and the corresponding 3-dB beamwidth and the first SLL are 0.084° and −7.6 dB, respectively. The AF with a Blackman window is shown in Figure 5c,h, the 3-dB beamwidth increases to 0.116°, while the first SLL decreases to −13.7 dB.

The simulation parameters of GeoSTAR are shown in Table 3. The simulation process of GeoSTAR consists of the following steps. First, similar to GMR, the coordinates of each pixel of the upwelling TB are converted from the latitude and longitude coordinate system to the direction cosine coordinate system of GeoSTAR to obtain $TB(\xi,\eta)$. Second, the measured visibility function is calculated according to Equations (4) and (5), and the system noise ΔT_{rms} is added. Third, the observed brightness temperature TA by GeoSTAR is reconstructed according to Equations (5) and (6), and the Blackman window is used. In addition, to mitigate the Gibbs oscillation effect, flat target transformation (FTT) is applied to the brightness temperature reconstruction process [45]. The simulated GeoSTAR observation TA images of Typhoon Hagibis for all 8 channels are shown in Figure 4a–h.

4.2.3. Geostationary Interferometric Microwave Sounder (GIMS)

GIMS is a new concept of an atmospheric microwave sounder for China's future geostationary microwave meteorological satellite (FY-4MW). GIMS is a 50–60 GHz SAIR working in rotating mode with a 70-element circular antenna array. Compared with a conventional stationary SAIR, the rotating SAIR can significantly reduce the number of elements required with the same array aperture at the cost of longer observation periods.

The optimized thinned array layout of GIMS is shown in Figure 7a. Seventy antennas sparsely distributed around a 3.7 m diameter circle form the required baselines. Although the snapshot UV plane samples are very sparse and irregular, as shown in Figure 7b, the full samples after a rotation cycle in Figure 7c provide good UV plane coverage. Comparing Figures 6d and 7d, it can be seen that the UV plane samples of GeoSTAR are in a hexagonal uniform grid, but the UV plane samples of GIMS are in a nonuniform polar grid. For the visibility function in the nonuniform polar grid, such a generalized IDFT algorithm does not exist to perform brightness temperature reconstruction.

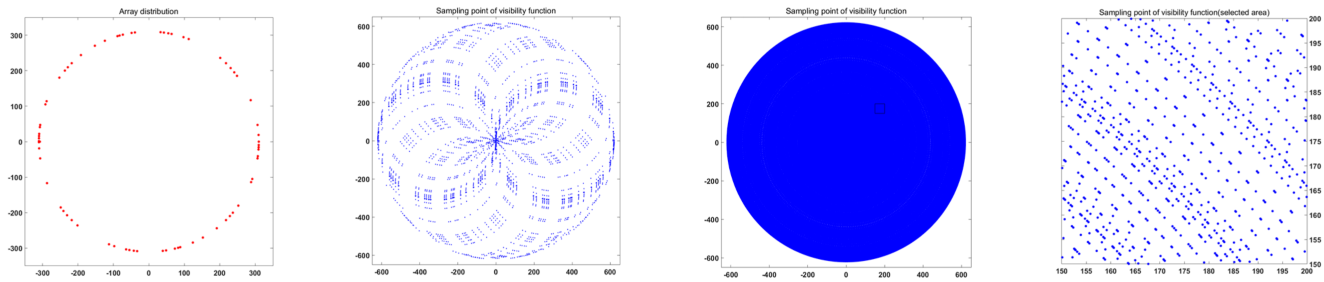

(**a**) (**b**) (**c**) (**d**)

Figure 7. The antenna array (**a**) and resulting UV plane sampling pattern of the GIMS. (**b**) Snapshot samples, (**c**) the full samples after a rotation cycle, and (**d**) partial zoomed-in view.

To solve this problem, the visibility samples of GIMS are interpolated from the polar grid to the pseudo polar grid, and then the inverse pseudo polar FFT (PPFFT) is used to reconstruct the brightness temperature distribution [46]. The pseudo polar grid is composed of the intersection nodes between concentric squares and equisloped rays, as shown in Figure 8a. The interpolation from the polar grid to the pseudo polar grid can be implemented by two 1-D interpolations, generally having higher accuracy than 2-D interpolations. For the polar grid of visibility, the equiangular sample points of each circle are 1-D interpolated in the angular direction to obtain equisloped points (as shown in Figure 8b), and then the sample points along each equisloped ray are 1-D interpolated again in the radial direction to square the circles and obtain the pseudo polar grid (as shown in Figure 8c). Finally, the inverse Fourier transform from the pseudo polar grid visibility samples in the spatial frequency domain to the brightness temperature distribution in the spatial domain can be quickly and accurately implemented by inverse PPFFT and the conjugate gradient method.

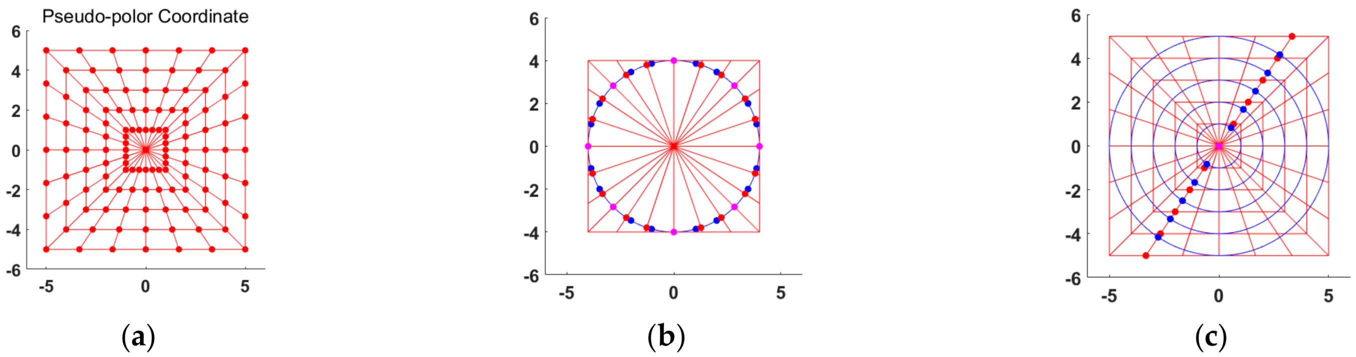

Figure 8. (**a**) Diagram of the pseudo polar grid. (**b**) Sketch of 1-D interpolations in the angular direction to obtain equisloped points. (**c**) Sketch of 1-D interpolations in the radial direction to square the circles.

Figure 5d,i shows the simulated 2-D and E-plane 1-D AF of the GIMS with a rectangular window at 50.3 GHz, and the corresponding 3-dB beamwidth and the first SLL are 0.064° and −8.8 dB, respectively. The AF with a Blackman window is shown in Figure 5e,j. The 3-dB beamwidth increases to 0.112°, while the first SLL decreases to −28.5 dB, consistent with GeoSTAR.

The simulation parameters of GIMS are shown in Table 3. The simulation process of GIMS is similar to GeoSTAR. The main difference is that the inverse PPFFT algorithm instead of inverse DFT is used to reconstruct the brightness temperature distribution from the visibility for the GIMS. The simulated GIMS observation TA images of Typhoon Hagibis for all 8 channels are shown in Figure 4i–p.

4.3. Comparison of Simulated Observation Brightness Temperature

Figure 5 shows the simulated antenna pattern of GMR and the synthetic AF of GeoSTAR and GIMS at 50.3 GHz. The top panels show the 2-D antenna pattern and AF, and the bottom panels show the 1-D antenna pattern and AF. Compared with the antenna pattern, the side lobe of the AF has a higher level and a negative value due to the Gibbs oscillation effect. The 2-D distribution of the side lobe of the AF depends on the UV plane sample grid, i.e., GeoSTAR has a hexagonal side lobe pattern, and GIMS has a circular sidelobe pattern. The Blackman window can effectively suppress the sidelobe level, but the main lobe width also increases significantly. Table 4 summarizes the main lobe and sidelobe characteristics of GMR, GeoSTAR, and GIMS, as well as radiometric sensitivity.

Figure 4 shows the simulated upwelling brightness temperature TB(a) and observation TA of GMR(b), GeoSTAR(c), and GIMS(d) for Typhoon *Hagibis* at 06:00 UTC on 8 October 2019. Figure 4A–H represents the 8 frequency channels in Table 2. The Blackman window is used for GeoSTAR and GIMS. For the relatively transparent channels, i.e., 1–4, the quality degradation of the TA images mainly come from the blurring caused by the limited main lobe beamwidth and side lobe, while for the opaque channels, i.e., channels 5–8, the TA image error is more from the system random noise. GeoSTAR, as a stationary SAIR, has the longest integration time in the simulation configuration, resulting in the smallest system noise. Thus, the TA images of the 5–8 channels appear to have the smallest error. Table 5 lists the root mean square error (RMSE) between the upwelling brightness temperature TB and observation TA of GMR, GeoSTAR, and GIMS for all 8 channels in Figure 4. The RMSEs are smaller at opaque channels 5–8 than at more transparent channels 1–4. Among the three instruments compared, GMR has the smallest error for more transparent channels 1–4, but the difference is not significant, and for opaque channels 5–8, GeoSTAR has the smallest error. Figure 9 shows the average RMSE of 13 TA images of Typhoon *Hagibis* from 06:00 to 12:00 UTC on 8 October 2019, used in the GEO-MW OSSE. It is clear that the RMSE results in Figure 9 are consistent with Table 5.

Table 4. Characteristics of GMR, GeoSTAR and GIMS at 50.3 GHz.

RMSE	3 dB Beamwidth (deg)	Ground Resolution (km)	First SLL (dB)	Sensitivity (K)
GMR	0.087	54	−24.6	0.33
GeoSTAR (rectangle)	0.084	52	−7.6	0.79
GeoSTAR (Blackman)	0.116	72	−13. 7	0.36
GIMS (rectangle)	0.064	40	−8.8	5.59
GIMS (Blackman)	0.112	70	−28.5	1.46

Table 5. RMSE(K) between the TB and the observation TA of GMR, GeoSTAR and GIMS.

RMSE	Ch1	Ch2	Ch3	Ch4	Ch5	Ch6	Ch7	Ch8
GMR	4.49	2.77	1.10	0.32	0.22	0.22	0.24	0.24
GeoSTAR	4.72	2.86	1.12	0.33	0.20	0.13	0.18	0.23
GIMS	4.80	2.94	1.23	0.56	0.45	0.42	0.42	0.45

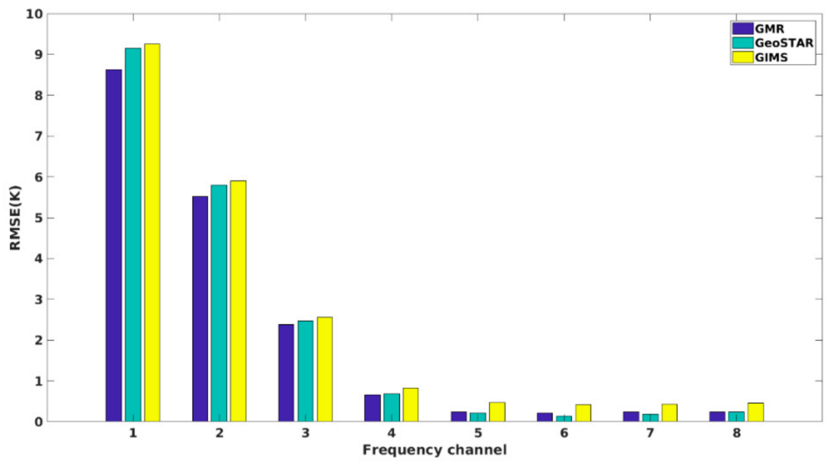

Figure 9. The average RMSE of 13 TA images of Typhoon Hagibis from 06:00 to 12:00 UTC on 8 October 2019.

5. GEO-MW OSSE Experimental Setup and Results

5.1. Data Assimilation Configurations and Experimental Design

The capability of assimilating GEO-MW brightness temperature observations was exploited in the WRF and WRFDA-4DVar systems to investigate their potential impact on the NWP of Typhoon Hagibis and Bualoi. Four parallel experiments were conducted, denoted CTRL, DA-GMR, DA-GeoSTAR, and DA-GIMS, respectively. Besides, the typhoon best track obtained from the CMA is called REAL. All of these are summarized in Table 6.

Table 6. Detailed description of the four experiments and REAL.

	Experiment	DA Scheme	Data	Spatial Resolution
1	CTRL	No DA	\	\
2	REAL	No DA	\	\
3	DA-GMR	Half-hourly 4D-Var DA	GMR	**52 km**
4	DA-GeoSTAR	Half-hourly 4D-Var DA	GeoSTAR	**74 km**
5	DA-GIMS	Half-hourly 4D-Var DA	GIMS	**70 km**

The control experiment, CTRL, assimilated no GEO-MW brightness temperature data, which directly predicts 72 h using initial and lateral boundary conditions provided by FNL reanalysis data, serving as a benchmark forecast compared with other GEO-MW data assimilation experiments. The assimilation experiments (DA-GMR, DA-GeoSTAR, and DA-GIMS corresponding to simulated observation TA of GMR, GeoSTAR, and GIMS, respectively) used the initial field of the CTRL as the background field and assimilated GEO-MW brightness temperature data at half-hourly time intervals within the six-hour time period to generate the analysis field. Then, the analysis field was used as a new initial for the 72 h prediction. The GEO-MW brightness temperature data assimilated in all experiments were thinned to a mesh of 60 km to reduce the impact of potential correlations among the observations. The REAL-track selected the 72 h best typhoon tracks of CMA starting from the assimilation time as the reference true value to evaluate the prediction error of the assimilation experiments. The sequence diagram of the 5 experiments is shown in Figure 10.

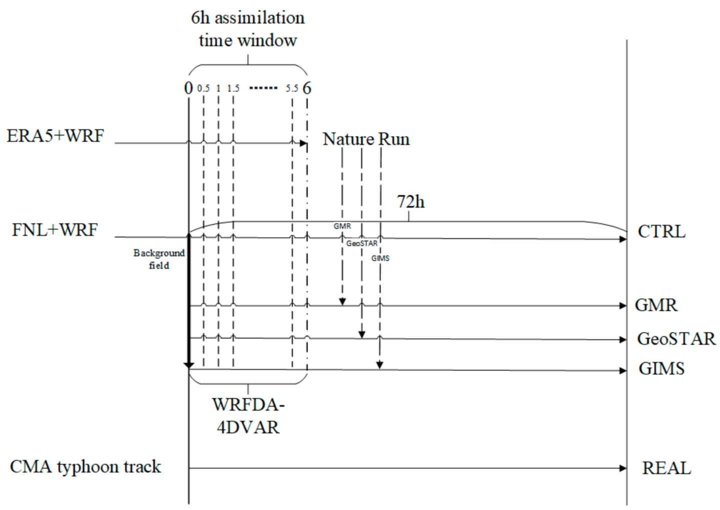

Figure 10. Sequence diagram of CTRL, REAL, DA-GMR, DA-GeoSTAR, and DA-GIMS experiments.

The WRFDA-4Dvar assimilation experimental parameter settings of Typhoons *Hagibis* and *Bualoi* are shown in Table 7. The GEO-MW brightness temperature data of *Hagibis* were simulated by the Nature Run data at half-hour intervals from 06:00 UTC to 12:00 UTC on 8 October. In the CTRL experiment of *Hagibis*, the 6-h short-term forecast field initialized with the FNL reanalysis data at 00:00 UTC on 8 October was used as the initial field for the 72-h WRF prediction to obtain the typhoon track from 06:00 UTC on 8 October to 06:00 UTC on 11 October. In the assimilation experiments, the analysis field at 06:00 UTC on 8 October was used as the initial field for the 72-h WRF prediction to obtain the typhoon track with the same time range as the CTRL experiment. The sequence of Typhoon *Bualoi* was similar to that of Hagibis, except the date was 22 October.

Table 7. The parameter settings of WRFDA-4Dvar assimilation experiments.

Typhoon Scene	Bualoi	Hagibis
Central latitude and longitude	22.5N 140E	22.5N 142.5E
Grid size	30 km × 30 km	
Number of grids	121 × 121	
Vertical stratification	42	
Top air pressure	10 hpa	
4Dvar time interval	0.5 h	
Assimilation time window area	6 h	
Radiative transfer mode	CRTM	
Frequency channel for assimilation	4, 5, 6, 8	
Assimilation moment	06:00 UTC on 8 October	06:00 UTC on 22 October

As future satellite data, GEO-MW brightness temperature data are not yet supported by the WRFDA. Therefore, to assimilate the GEO-MW observation data using the WRFDA-4Dvar system, it is necessary to first convert it into a BUFR (binary universal form of the representation of meteorological data, see more details in https://noaa-emc.github.io/NCEPLIBS-bufr/ (accessed on 21 March 2021)) format file supported by the WRFDA. In this study, a Fortran script was developed to compile the simulated GEO-MW brightness temperature data into the BUFR format files of AMSUA using BUFRLIB (see more details in https://github.com/NOAA-EMC/NCEPLIBS-bufr (accessed on 21 March 2021)). This approach is a shortcut to assimilate simulated future observations using the WRFDA system, with the advantage that the data preprocessing steps, including quality control, data thinning, and bias correction, can be consistent with existing operational data assimilation schemes.

In this study, the quality control procedures of AMSUA in WRFDA were applied to the GEO-MW brightness temperature data, including surface type check, absolute and relative departure check, cloud check, and rain check. Finally, only four channels of GEO-MW brightness temperature data, 4 to 6 and 8, could be assimilated by the WRFDA system.

5.2. Experimental Results

The scatter plots of model-calculated brightness temperatures versus the assimilated GEO-MW observations of Typhoon Hagibis valid at 06:00 UTC on 8 October, 2019 for GMR, GeoSTAR, and GIMS are shown in Figures 11–13, respectively. The top panels of each figure show the background-calculated brightness temperature versus the GEO-MW observations. The bottom panels show the analysis-calculated brightness temperature data versus the observations. After assimilating the GEO-MW brightness temperature data, the analysis results had closer agreements with the observations than the background, i.e., the RMSEs of channels 4–6 and 8 for GMR were reduced by approximately 6%, 10%, 7%, and 26%, respectively (Figure 11), the RMSEs of channels 4–6 and 8 for GeoSTAR were reduced by approximately 14%, 28%, 20%, and 2%, respectively (Figure 12), and the RMSEs of channels 4–6 and 8 for GIMS were reduced by approximately 9%, 7%, 7%, and 23%, respectively (Figure 13), indicating that the WRFDA-4Dvar was effective in directly assimilating the simulated GEO-MW brightness temperature data. Table 8 show lists the RMSEs (K) of brightness temperature calculated from the background field and analysis field versus the relative to observation.

The verification of typhoon track forecasts for CTRL, DA-GMR, DA-GeoSTAR, and DA-GIMS experiments are discussed in this subsection. The best track data (REAL) were provided by the TCDC of CMA. The 72-h best track of Typhoon Hagibis and the predicted tracks of four experiments (CTRL, DA-GMR, DA-GeoSTAR, and DA-GIMS) initialized from 06:00 UTC on 8 October are shown in Figure 14a, and Figure 14b shows the forecasting track error against the best track data. For Hagibis, in the first 30 h, the locations of the typhoon's center in the CTRL and three DA experiments were close to the observed locations, and there is no clear difference between the CTRL and the three DA experiments. The predicted tracks began to diverge from the best track after 30 h, and from 30 h onward, the track forecasts given by the three DA experiments were consistently better than those given by CTRL. Of the three DA experiments, from 30 h onward, the predicted track of DA-GeoSTAR was consistently the closest to the best track, followed by DA-GMR, and the track forecast given by DA-GIMS had the largest deviation.

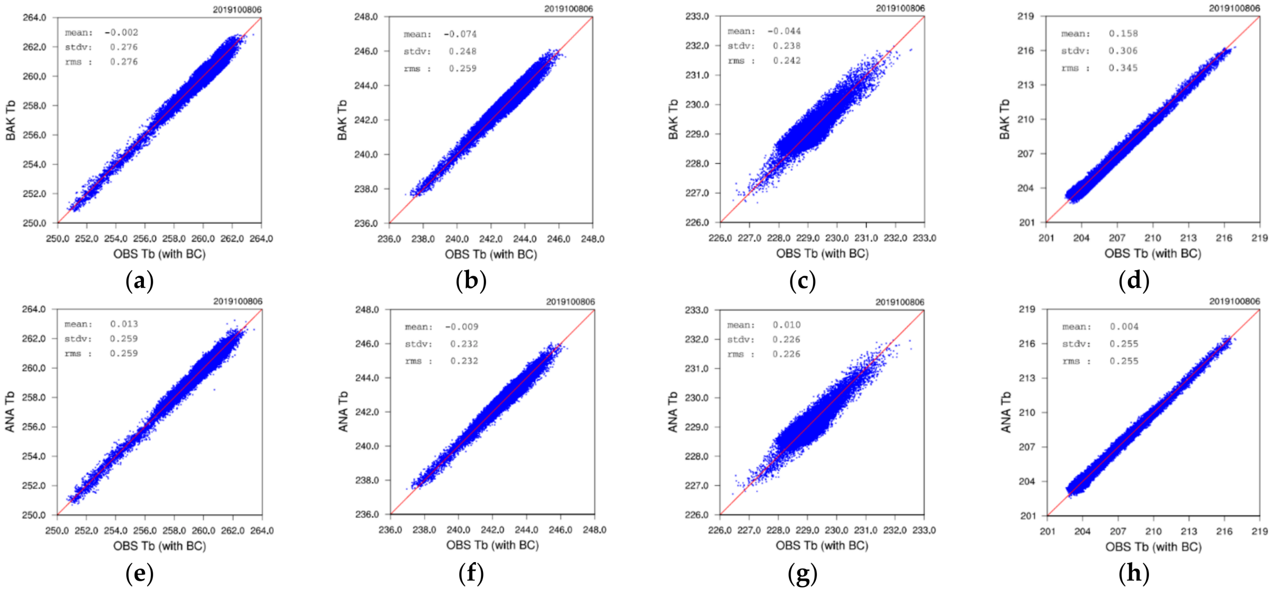

Figure 11. Scatter plots of model-calculated brightness temperature versus the observations (K) of GMR for (**a**–**d**) background and (**e**–**h**) analyses valid at 06:00 UTC on 8 October 2019. (**a**,**e**) represents channel-4 53.596 GHz, (**b**,**f**) represents channel-5 54.4 GHz, (**c**,**g**) represents channel-6 54.94 GHz, and (**d**,**h**) represents channel-8 57.29 GHz.

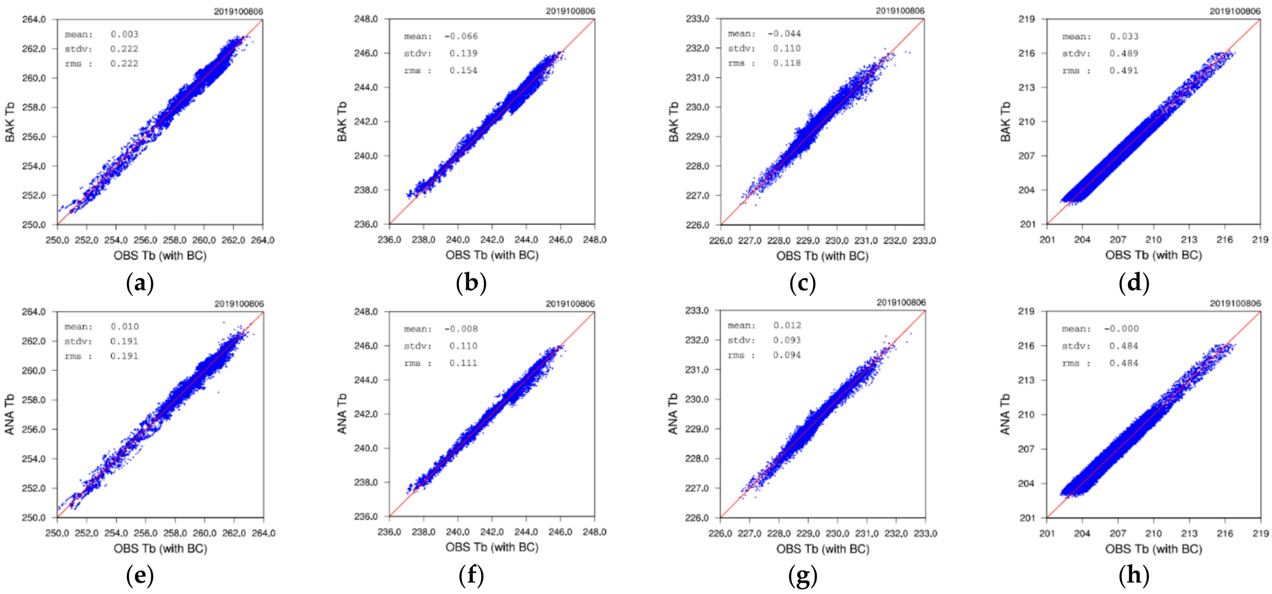

Figure 12. Scatter plots of model-calculated brightness temperature versus the observations (K) of GeoSTAR for (**a**–**d**) background and (**e**–**h**) analyses valid at 06:00 UTC on 8 October 2019. (**a**,**e**) represents channel-4 53.596 GHz, (**b**,**f**) represents channel-5 54.4 GHz, (**c**,**g**) represents channel-6 54.94 GHz, and (**d**,**h**) represents channel-8 57.29 GHz.

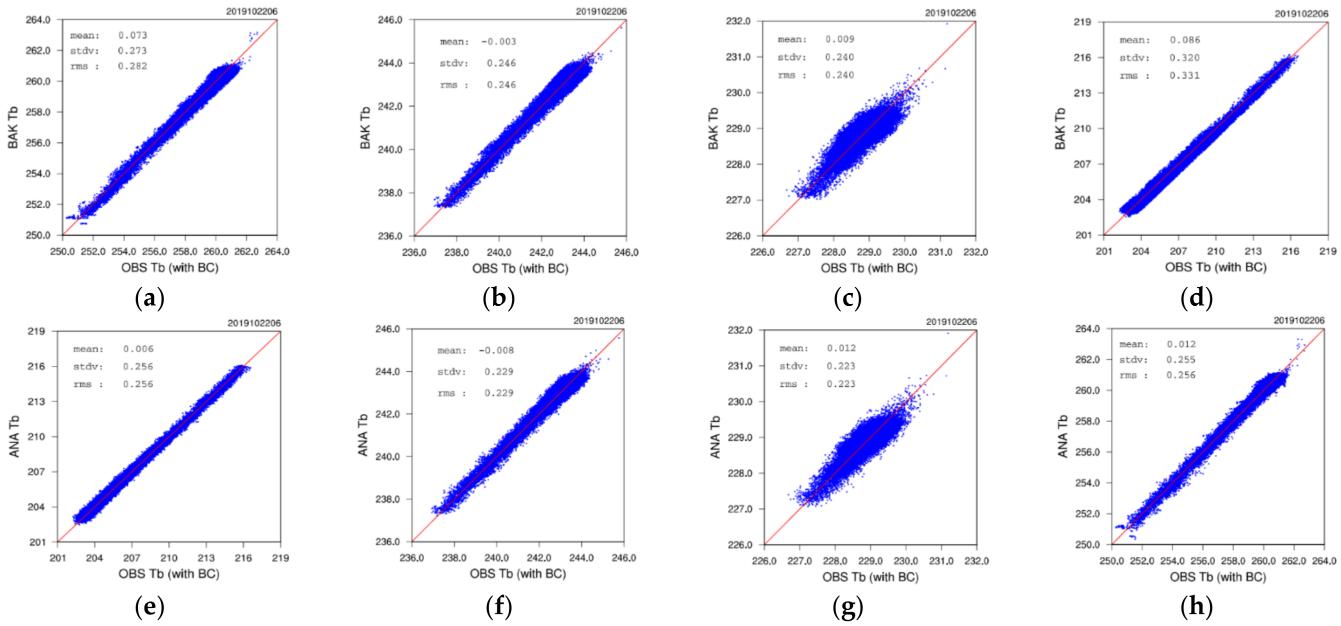

Figure 13. Scatter plots of model-calculated brightness temperature versus the observations (K) of GIMS for (**a**–**d**) background and (**e**–**h**) analyses valid at 06:00 UTC on 8 October 2019. (**a**,**e**) represents channel-4 53.596 GHz, (**b**,**f**) represents channel-5 54.4 GHz, (**c**,**g**) represents channel-6 54.94 GHz, and (**d**,**h**) represents channel-8 57.29 GHz.

Table 8. RMSE (K) of brightness temperature calculated from background field and analysis field relative to observation.

RMSE		53.596 GHZ	54.4 GHz	54.94 GHz	57.29 GHz
GMR	background field	0.276	0.259	0.242	0.345
	analysis field	0.259	0.232	0.226	0.255
GeoSTAR	background field	0.222	0.154	0.118	0.491
	analysis field	0.191	0.111	0.094	0.484
GIMS	background field	0.282	0.246	0.24	0.331
	analysis field	0.256	0.229	0.223	0.256

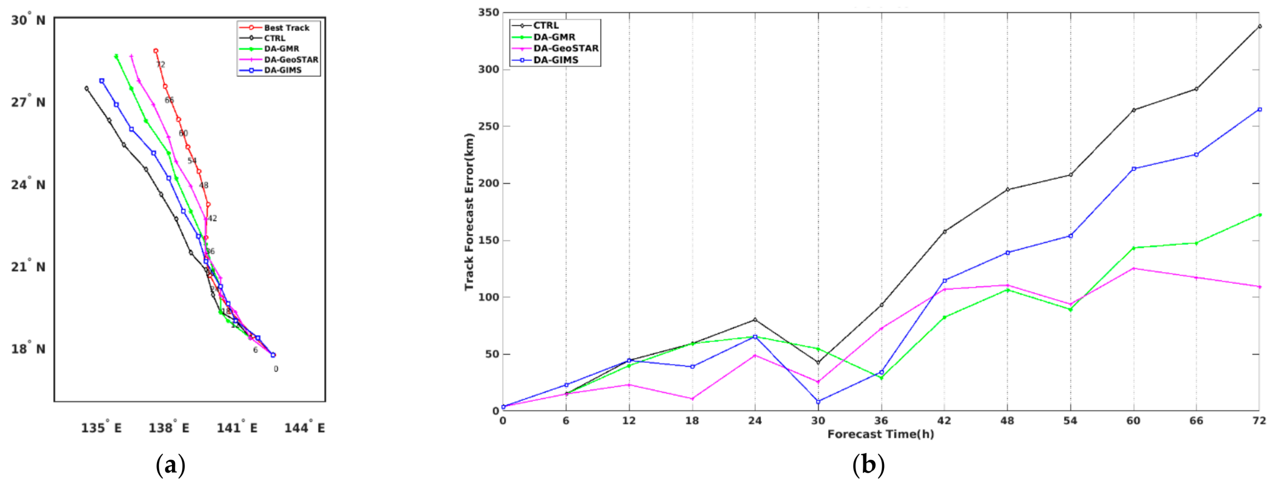

Figure 14. The predicted track of Hagibis initialized from 06:00 UTC on 8 October 2019 (**a**) and track forecast errors (**b**). The red curve in (**a**) represents the best typhoon track data.

Figure 15 shows the 72-h best track, and the predicted tracks of Typhoon *Bualoi* initialized from 06:00 UTC on 22 October and the forecasting track error. For *Bualoi*, in the first 18 h, the locations of the typhoon's center in CTRL were close to those in the three DA experiments. The predicted tracks began to diverge from the best track after 6 h, and from 18 h onward, the track forecasts given by the three DA experiments were consistently better than those given by CTRL. Of the three DA experiments, from 18 h onward, the predicted track of DA-GeoSTAR was consistently the closest to the best track, followed by DA-GMR, and the track forecast given by DA-GIMS still had the largest deviation.

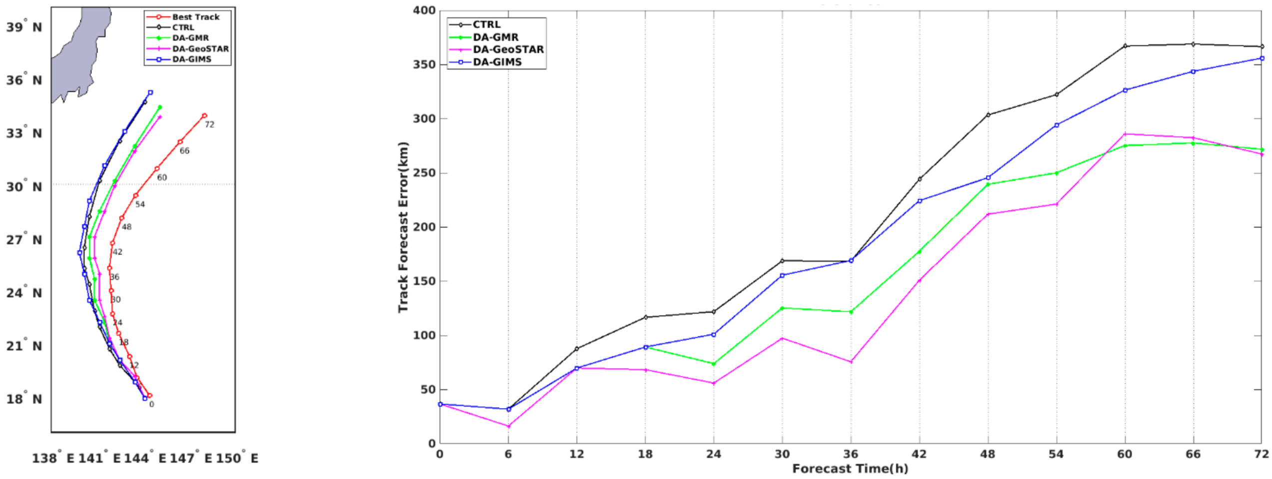

(**a**) (**b**)

Figure 15. The predicted track of Bualoi initialized from 06:00 UTC on 22 October 2019 (**a**) and track forecast errors (**b**). The red curve in (**a**) represents the best typhoon track data.

Table 9 presents the average typhoon track forecast performance of the different experiments. Due to the limited accuracy of WRF, we have rounded the results to 10 km. Compared with CTRL, for *Bualoi* and *Hagibis*, DA-GMR improved the average 72-h typhoon track forecast accuracy by 24% and 43%, DA-GeoSTAR by 33% and 50%, and DA-GIMS by 10% and 29%, respectively. Table 10 presents the 72-h typhoon track forecast performance of the different experiments. Compared with CTRL, for *Bualoi* and *Hagibis*, DA-GMR improved the average 72-h typhoon track forecast accuracy by 27% and 50%, DA-GeoSTAR by 27% and 68%, and DA-GIMS by 3% and 21%, respectively. CTRL without any data assimilation generated the worst results, DA-GeoSTAR obtained the best performance, followed by DA-GMR, and DA-GIMS had the largest track error in the three DA experiments. The consistent results in both Typhoons *Hagibis* and *Bualoi* suggest general positive impacts on typhoon forecasts after assimilating the simulated GEO-MW observations of GMR, GeoSTAR, and GIMS in the OSSE experiments. The difference among the typhoon track forecast performances of the three assimilation experiments may be related to the observed brightness temperatures errors of GMR, GeoSTAR, and GIMS. As described in Section 4.3, for opaque channels 4–6 and 8 used in assimilation experiments, the observed brightness temperature error is more from the random noise of the system. GeoSTAR, as a stationary SAIR, has the longest integration time in the simulation configuration, resulting in the smallest system noise. From Table 5 and Figure 9, it can be seen that GeoSTAR had the smallest overall brightness temperature error for channels 4–6 and 8, followed by GMR, and GIMS had the largest error. The relatively large brightness temperature error of GIMS mainly came from the shorter integration time due to array rotation, and the error introduced by the interpolation of the UV plane visibility may also slightly degrade the quality of the reconstructed brightness temperature.

Table 9. The average error of the predicted track.

Track Error (km)	CTRL	DA-GMR	DA-GeoSTAR	DA-GIMS
Hagibis	140	80	70	100
Bualoi	210	160	140	190

Table 10. The 72-h error of the predicted track.

Track Error (km)	CTRL	DA-GMR	DA-GeoSTAR	DA-GIMS
Hagibis	340	170	110	270
Bualoi	370	270	270	360

6. Summary

At present, GMR with a 5 m real aperture antenna, GeoSTAR with a stationary Y-shape synthetic aperture array, and GIMS with a rotating circular synthetic aperture array are three promising solutions for GEO-MW sounders. The objective of this study was to provide preliminary results on the potential impact of assimilation of the GEO-MW observations of GMR, GeoSTAR, and GIMS at 50–60 GHz on typhoon prediction. The GEO-MW OSSEs were performed using the WRF model and WRFDA-4DVar assimilation system for Typhoons *Hagibis* and *Bualoi*.

New 50–60 GHz observed brightness temperature data from GMR, GeoSTAR, and GIMS onboard a geostationary satellite were simulated from the Nature Run obtained from the ERA-5 reanalysis data and WRF forecast. The brightness temperature observation capabilities of GMR, GeoSTAR, and GIMS for 8 channels at 50–60 GHz were analyzed. Data assimilation produced analyses and forecasts for GMR, GeoSTAR, and GIMS, using the WRFDA-4DVar assimilation system. The forecast errors in the typhoon track were computed against the best typhoon track data from the tropical cyclone data center of CMA.

Verification against the control experiment showed that the experiment with the assimilated GEO-MW data gave a consistently more accurate prediction of the track for Typhoons *Hagibis* and *Bualoi*. The assimilation of the three GEO-MW instruments with channels 4–6 and 8 at 50–60 GHz could have led to the general positive impacts in this study. However, these positive impacts seemed to depend on the observation error of the three potential instruments. For both Typhoons *Hagibis* and *Bualoi*, GeoSTAR obtained the best assimilation effect, followed by GMR, and GIMS had the largest track error. For opaque channels 4–6 and 8 used in assimilation experiments, the observed brightness temperature error was mainly due to the random system noise. GeoSTAR, as a stationary SAIR, had the longest integration time in the simulation configuration, resulting in the smallest observation error in channels 4–6 and 8. GIMS, as a rotating SAIR, was set for a shorter integration time, and the interpolation of the UV plane visibility may have also slightly increased the reconstructed brightness temperature error, which resulted in the largest observation error.

This is the first study to compare the three geostationary microwave sounders, GMR, GeoSTAR, and GIMS, in the GEO-MW OSSEs. Only preliminary results for two cases have been provided. To further consolidate the conclusions drawn here, more experiments concerning different cases are needed. In addition, the relationship between the brightness temperature observation capability and the impact of assimilation of different GEO-MW observation system configurations will be explored further in future studies.

Author Contributions: Writing—original draft: K.C. and G.W. All authors have read and agreed to the published version of the manuscript.

Funding: This research was supported by Shanghai Aerospace Science and Technology Foundation of Shanghai Academy of Spaceflight Technology (SAST2019-102).

Institutional Review Board Statement: Not applicable.

Informed Consent Statement: Not applicable.

Data Availability Statement: The data used to support the findings of this study are available from the corresponding author upon request.

Acknowledgments: The authors thank editors and anonymous reviewers for their constructive comments and useful suggestions that significantly improved the manuscript. The authors thank the NSSC, CSA for providing the GIMS antenna array layout. The authors also thank SAETI for providing the system parameters of GMR. The authors also thank ECMWF for providing the ERA-5 reanalysis data and NCEP for sharing the FNL reanalysis data. The authors also thank the NCAR for sharing the WRF and WRFDA codes.

Conflicts of Interest: The authors declare no conflict of interest.

References

1. Kazumori, M.; Liu, Q.; Treadon, R.; Derber, J. Impact Study of AMSR-E Radiances in the NCEP Global Data Assimilation System. *Mon. Weather Rev.* **2008**, *136*, 541–559. [CrossRef]
2. Zou, X.; Weng, F.; Zhang, B.; Lin, L.; Qin, Z.; Tallapragada, V. Impacts of assimilation of ATMS data in HWRF on track and intensity forecasts of 2012 four landfall hurricanes. *J. Geophys. Res. Atmos.* **2013**, *118*, 11558–11576. [CrossRef]
3. Zhang, H.; Xue, J.; Zhu, G.; Zhuang, S.; Wu, X.; Zhang, F. Application of direct assimilation of ATOVS microwave radiances to typhoon track prediction. *Adv. Atmos. Sci.* **2004**, *21*, 283–290. [CrossRef]
4. Zhu, G.; Xue, J.; Zhang, H.; Lin, Z.; Zhuang, S.; Huang, L.; Dong, P. Direct assimilation of satellite radiance data in GRAPES variational assimilation system. *Chin. Sci. Bull.* **2008**, *53*, 3465–3469. [CrossRef]
5. Yang, C.; Zhu, L.; Min, J. Impact Study of FY-3B MWRI Data Assimilation in WRFDA. *Atmosphere* **2021**, *12*, 497. [CrossRef]
6. Weng, F.; Zou, X.; Wang, X.; Yang, S.; Goldberg, M. Introduction to Suomi national polar-orbiting partnership advanced technology microwave sounder for numerical weather prediction and tropical cyclone applications. *J. Geophys. Res.* **2012**, *117*, D19112. [CrossRef]
7. Lu, N.; Gu, S. The status and prospects of atmospheric microwave sounding by geostationary meteorological satellite. *Adv. Meteorol. Sci. Tech.* **2016**, *6*, 120–123.
8. Laganà, A.; Iero, D.; Isernia, T.; Morabito, A.; Carlström, A.; Toso, G. On the design and optimization of the array elements in the GEO Atmospheric Sounder instrument A new design procedure. In Proceedings of the 2010 IEEE International Geoscience and Remote Sensing Symposium (IGARSS), Honolulu, HI, USA, 25–30 July 2010; pp. 578–581.
9. Xie, Z.; Xue, H.; An, D.; He, J.; Zhang, D.; Zhu, Z. Remote sensing technology of experimental microwave radiometer in geostationary orbit. *Aerospace Shanghai* **2018**, *35*, 49–59.
10. Chen, K.; Zheng, Z.; Cai, B.; An, D.; Xie, Z.; Li, Z. Performance of geostationary orbit millimeter-wave atmospheric soundings based on end to end simulations. *J. Infrared Millim. Waves* **2021**, *40*, 230–242.
11. Solman, F.; Staelin, D.; Kerekes, J.; Shields, M. A microwave instrument for temperature and humidity sounding from geosynchronous orbit. In Proceedings of the 1998 IEEE International Geoscience and Remote Sensing Symposium (IGARSS), Seattle, WA, USA, 6–10 July 1998; pp. 1704–1707.
12. Bizzarri, B.; Gasiewski, A.; Staelin, D. Initiatives for millimetre/submillimetre-wave sounding from geostationary orbit. In Proceedings of the 2002 IEEE International Geoscience and Remote Sensing Symposium (IGARSS), Toronto, ON, Canada, 24–28 June 2002; pp. 548–552.
13. Gasiewski, A. GOMAS Geostationary Observatory for Microwave Atmospheric Sounding. In Proceedings of the 2002 International TO VS Study Conference (ITSC), Lorne, Australia, 27 February–5 March 2002.
14. Gasiewski, A.; Voronovich, A.; Weber, B.; Stankov, B.; Klein, M.; Hill, R.; Bao, J. Geosynchronous microwave (GEM) sounder/imager observation system simulation. In Proceedings of the 2003 IEEE International Geoscience and Remote Sensing Symposium (IGARSS), Toulouse, France, 21–25 July 2003; pp. 1209–1211.
15. Wang, Y.; Kang, A.; Cao, Y.; Jiang, S. Research of real aperture microwave antenna main reflector thermal control measures on geostationary earth orbit. *Aerosp. Shanghai* **2016**, *33*, 107–113.
16. Xie, Z.; Li, X.; Yao, C.; Jiang, L.; Li, X. Research on geostationary orbit microwave radiometer technology. *Aerosp. Shanghai* **2018**, *35*, 20–28.
17. Le Vine, D.; Kao, M.; Tanner, A.; Swift, C.; Griffis, A. Initial results in the development of a synthetic aperture microwave radiometer. *IEEE Trans. Geosci. Remote* **1990**, *28*, 614–619. [CrossRef]
18. Ruf, C. Error analysis of image reconstruction by a synthetic aperture interferometric radiometer. *Radio Sci.* **1991**, *26*, 1419–1434. [CrossRef]
19. Tanner, A.; Wilson, W.; Kangaslahti, P.; Lambrigsten, B.; Dinardo, S.; Piepmeier, J.; Musko, S. Prototype development of a geostationary synthetic thinned aperture radiometer, GeoSTAR. In Proceedings of the 2004 IEEE International Geoscience and Remote Sensing Symposium (IGARSS), Anchorage, AK, USA, 20–24 September 2004; pp. 1256–1259.
20. Zhang, C.; Liu, H.; Wu, J.; Zhang, S.; Yan, J.; Niu, L.; Sun, W.; Li, H. Imaging analysis and first results of the geostationary interferometric microwave sounder demonstrator. *IEEE Trans. Geosci. Remote* **2015**, *53*, 207–218. [CrossRef]

21. Tanner, A.; Wilson, W.; Lambrigtsen, B.; Dinardo, S.; Brown, S.; Kangaslahti, P.; Gaier, T.; Ruf, C.; Gross, S.; Lim, B.; et al. Performance evaluation of the Geostationary Synthetic Thinned Array Radiometer (GeoSTAR) demonstrator instrument. *IEEE Trans. Geosci. Remote* **2007**, *45*, 1947–1957. [CrossRef]
22. Lambrigtsen, B.; Brown, S.; Gaier, T.; Herrell, L.; Kangaslahti, P.; Tanner, A. Monitoring the hydrologic cycle with the PATH mission. *Proc. IEEE* **2010**, *98*, 862–877. [CrossRef]
23. Gaier, T.; Lambrigtsen, B.; Kangaslahti, P.; Lim, B.; Tanner, A.; Harding, D.; Owen, H.; Soria, M.; O'Dwyer, L.; Ruf, C. GeoSTAR-II: A prototype water vapor imager/sounder for the PATH mission. In Proceedings of the 2011 IEEE International Geoscience and Remote Sensing Symposium (IGARSS), Vancouver, BC, Canada, 24–29 July 2011; pp. 3626–3628.
24. Gaier, T.; Kangaslahti, P.; Lambrigtsen, B.; Ramos-Perez, I.; Tanner, A.; McKague, D.; Ruf, C.; Flynn, M.; Zhang, Z.; Backhus, R.; et al. A 180 GHz prototype for a geostationary microwave imager/sounder-GeoSTAR-III. In Proceedings of the 2016 IEEE International Geoscience and Remote Sensing Symposium (IGARSS), Beijing, China, 10–15 July 2016; pp. 2021–2023.
25. Zhang, Y.; Liu, H.; Wu, J.; He, J.; Zhang, C. Statistical analysis for performance of detection and imaging of dynamic targets using the geostationary interferometric microwave sounder. *IEEE J. Sel. Top. Appl. Earth Obs. Remote Sens.* **2018**, *11*, 3–11. [CrossRef]
26. Liu, H.; Niu, L.; Zhang, C.; Han, D.; Lu, H.; Zhao, X.; Wu, J. Preliminary results of GIMS-II (Geostationary interferometric microwave sounder-second generation) demonstrator. In Proceedings of the 2017 IEEE International Geoscience and Remote Sensing Symposium (IGARSS), Fort Worth, TX, USA, 23–28 July 2017; pp. 711–714.
27. Han, D.; Liu, H.; Wu, J.; Zhang, C.; Niu, L.; Zhang, Y. Interelement phase calibration for the geostationary interferometric microwave sounder (GIMS). *IEEE Geosci. Remote Sens.* **2016**, *13*, 1216–1220. [CrossRef]
28. Xue, J. Scientific issues and perspective of assimilation of meteorological satellite data. *Acta Meteorol. Sin.* **2009**, *67*, 903–911.
29. Chen, K.; Hong, P.; Han, W.; Li, Z.; Wang, H.; Wang, J.; Chen, H.; Zhang, Z.; Xie, Z. Geostationary microwave observation system simulation experiments using the GRAPES 4D-Var. *Acta Meteorol. Sin.* **2021**, *79*, 769–785.
30. Atlas, R.; Hoffman, R.; Ma, Z.; Emmitt, G.; Wood, S.; Greco, S.; Tucker, S.; Bucci, L.; Annane, B.; Hardesty, R.M.; et al. Observing System Simulation Experiments (OSSEs) to Evaluate the Potential Impact of an Optical Autocovariance Wind Lidar (OAWL) on Numerical Weather Prediction. *J. Atmos. Ocean. Technol.* **2015**, *32*, 1593–1613. [CrossRef]
31. Leidner, S.; Nehrkorn, T.; Henderson, J.; Mountain, M.; Tunck, T.; Hoffman, R. A Severe Weather Quick Observing System Simulation Experiment (QuickOSSE) of Global Navigation Satellite System (GNSS) Radio Occultation (RO) Superconstellations. *Mon. Weather Rev.* **2017**, *145*, 637–651. [CrossRef]
32. Wang, Y.; He, J.; Chen, Y.; Min, J. The Potential Impact of Assimilating Synthetic Microwave Radiances Onboard a Future Geostationary Satellite on the Prediction of Typhoon Lekima Using the WRF Model. *Remote Sens.* **2021**, *13*, 886. [CrossRef]
33. Zhang, K.; Gasiewski, A. Microwave CubeSat fleet simulation for hydrometric tracking in severe weather. In Proceedings of the 2016 IEEE International Geoscience and Remote Sensing Symposium (IGARSS), Beijing, China, 10–15 July 2016; pp. 5569–5572.
34. Duruisseau, F.; Chambon, P.; Guedj, S.; Guidard, V.; Fourrié, N.; Taillefer, F.; Brousseau, P.; Mahfouf, J.-F.; Roca, R. Investigating the potential benefit to a mesoscale nwp model of a microwave sounder on board a geostationary satellite. *Q. J. R. Meteorol. Soc.* **2017**, *143*, 2104–2115. [CrossRef]
35. Hersbach, H.; Bell, B.; Berrisford, P.; Hirahara, S.; Horányi, A.; Muñoz-Sabater, J.; Nicolas, J.; Peubey, C.; Radu, R.; Schepers, D.; et al. The ERA-5 global reanalysis. *Q. J. R. Meteorol. Soc.* **2020**, *146*, 1999–2049. [CrossRef]
36. National Centers for Environmental Prediction/National Weather Service/NOAA/U.S. *Department of Commerce, 2000: NCEP FNL Operational Model Global Tropospheric Analyses, Continuing from July 1999. Research Data Archive at the National Center for Atmospheric Research*; Computational and Information Systems Laboratory: Boulder, CO, USA, 2016.
37. Ying, M.; Zhang, W.; Yu, H.; Lu, X.; Feng, J.; Fan, Y.; Zhu, Y.; Chen, D. An overview of the China Meteorological Administration tropical cyclone database. *J. Atmos. Ocean. Technol.* **2014**, *31*, 287–301. [CrossRef]
38. Lu, X.; Yu, H.; Ying, M.; Zhao, B.; Wan, R. Western north pacific tropical cyclone database created by the China Meteorological Administration. *Adv. Atmos. Sci.* **2021**, *38*, 690–699. [CrossRef]
39. Gauthier, P.; Tanguay, M.; Laroche, S.; Pellerin, S.; Morneau, J. Extension of 3dvar to 4dvar: Implementation of 4dvar at the meteorological service of Canada. *Mon. Weather Rev.* **2010**, *135*, 2339–2354. [CrossRef]
40. Lorenc, A.; Rawlins, F. Why does 4D-Var beat 3D-Var? *Q. J. R. Meteorol. Soc.* **2005**, *131*, 3247–3257. [CrossRef]
41. Xiao, H.; Han, W.; Wang, H.; Wang, J.; Liu, G.; Xu, C. Impact of MWRI radiance assimilation in GRAPES 4DVar on Typhoon Shanshan forecasts. *J. Meteor. Res.* **2020**, *34*, 1–15. [CrossRef]
42. Chen, Y.; Weng, F.; Han, Y.; Liu, Q. Validation of the Community Radiative Transfer Model by using CloudSat data. *J. Geophys. Res.* **2008**, *113*, D00A03. [CrossRef]
43. Weng, F.; Zou, X.; Sun, N.; Yang, H.; Tian, M.; Blackwell, W.; Wang, X.; Lin, L.; Anderson, K. Calibration of Suomi national polar-orbiting partnership advanced technology microwave sounder. *J. Geophys. Res. Atmos.* **2013**, *118*, 11187–11200. [CrossRef]
44. Corbella, I.; Duffo, N.; Vall-llossera, M.; Camps, A.; Torres, F. The Visibility Function in Interferometric Aperture Synthesis Radiometry. *IEEE Geosci. Remote Sens.* **2004**, *42*, 1677–1682. [CrossRef]
45. Martin-Neira, M.; Suess, M.; Kainulainen, J.; Martin-Porqueras, F. The flat target transformation. *IEEE Geosci. Remote Sens.* **2008**, *46*, 613–620. [CrossRef]
46. Zhang, C.; Wu, J.; Sun, W. Applications of pseudo-polar FFT in synthetic aperture radiometer imaging. *Piers Online* **2007**, *3*, 25–30. [CrossRef]